Letter

Flat topological bands and eigenstate criticality in a quasiperiodic insulator

Yixing Fu,[1] Justin H. Wilson,[1] and J. H. Pixley[1,2,3]

[1]*Department of Physics and Astronomy, Center for Materials Theory, Rutgers University, Piscataway, New Jersey 08854, USA*
[2]*Center for Computational Quantum Physics, Flatiron Institute, 162 5th Avenue, New York, New York 10010, USA*
[3]*Physics Department, Princeton University, Princeton, New Jersey 08544, USA*

(Received 14 April 2020; revised 11 April 2021; accepted 25 June 2021; published 15 July 2021)

The effects of downfolding a Brillouin zone can open gaps and quench the kinetic energy by flattening bands. Quasiperiodic systems are extreme examples of this process, which leads to new phases and critical eigenstates. We analytically and numerically investigate these effects in a two-dimensional topological insulator with a quasiperiodic potential and discover a complex phase diagram. We study the nature of the resulting eigenstate quantum phase transitions; a quasiperiodic potential can make a trivial insulator topological and induce topological insulator-to-metal phase transitions through a unique universality class distinct from random systems. This wealth of critical behavior occurs concomitantly with the quenching of the kinetic energy, resulting in flat topological bands that could serve as a platform to realize the fractional quantum Hall effect without a magnetic field.

DOI: 10.1103/PhysRevB.104.L041106

Introduction. The interplay of topology and strong correlations produces fascinating phenomena, with the fractional quantum Hall effect [1] serving as the quintessential example. Conventionally, the magnetic field induces topology in the electronic many-body wave function; however, Berry curvature of the band structure is sufficient to induce topological single-particle wave functions that can survive the presence of interactions (see Ref. [2] for a review). Despite strong numerical evidence of fractional Chern and $\mathbb{Z}_2$ insulators [3–8], identifying a clear experimental route to the many-body analog of the fractional quantum Hall effect without a magnetic field remains challenging. Research in this direction has aimed to identify lattices with flat topological bands that quench the kinetic energy, promoting strong correlations [9–15].

Recent work on twisted graphene heterostructures opened up new platforms to study strongly correlated physics, including correlated insulators [16], superconductivity [17,18], and Chern insulators [19–21]. Proposals for realizing flat topological bands in these systems have followed [22–30]. It was also recently shown in Refs. [31,32] that the incommensurate effect of the twist could be emulated by a quasiperiodic potential. Consequently, a class of models, dubbed magic-angle semimetals, show similar phenomena to twisted bilayer graphene (e.g., the formation of minibands and the vanishing Dirac cone velocity) at or near an eigenstate phase transition. Similarly, to understand the theory for fractional Chern and $\mathbb{Z}_2$ insulators in incommensurate systems and how eigenstate criticality plays a role, it is essential to build a simple model to theoretically study and experimentally realize. The notion of flat band engineering with incommensuration has broad applicability outside twisted heterostructures, including ultracold atomic gases [33–35] and metamaterials [36–39].

In this Letter, we study a minimal model for a two-dimensional topological insulator (TI) with a quasiperiodic potential to find a controllable route to create flat topological bands and induce quantum phase transitions beyond the Landau-Ginzburg paradigm, as there is no spontaneous symmetry breaking involved. These transitions represent a universality class beyond the Altland-Zirnbauer classification of random matrices for disordered systems [40,41]. While the study of new metallic phases with quasiperiodicity came into focus with Refs. [42,43], the existing work on topology in nonperiodic systems focused on the topological to normal insulator transition [44,45] and appearance of finite energy topological bands [6,46]. Using analytic and numeric techniques we unite these ideas and find an intricate phase diagram, as shown in Fig. 1. Particularly, quasiperiodicity creates practically flat topological bands near where finite-energy states exhibit criticality. At the transition between topological and trivial insulators, the system realizes a magic-angle semimetal with features previously studied [31]. We further characterize the critical properties of the various eigenstate transitions, understanding them as localization and delocalization transitions in momentum- or real-space bases. Importantly, these transitions and phases could be directly realized in twisted bilayer graphene that is close to aligned with a hexagonal boron nitride substrate [47–49].

Model. To describe a two-dimensional topological insulator, we use the Bernevig-Hughes-Zhang (BHZ) model [50] with a two-dimensional (2D) quasiperiodic potential. The square-lattice Hamiltonian (with sites $\mathbf{r}$) is block diagonal,

$$\mathcal{H} = \sum_{\mathbf{r},\mathbf{r}'} c^\dagger_{\mathbf{r}'} \begin{pmatrix} h_{\mathbf{r}'\mathbf{r}} & 0 \\ 0 & h^*_{\mathbf{r}'\mathbf{r}} \end{pmatrix} c_{\mathbf{r}} + \sum_{\mathbf{r}} c^\dagger_{\mathbf{r}} V(\mathbf{r}) c_{\mathbf{r}}, \qquad (1)$$

where $c_{\mathbf{r}}$ are four-component annihilation operators and $V(\mathbf{r}) = W \sum_{\mu=x,y} \cos(Q r_\mu + \phi_\mu)$ is the quasiperiodic potential (QP) with amplitude W, wave vector Q, and random phase ϕ_μ; $h_{\mathbf{r}'\mathbf{r}}$ is a two-by-two matrix describing one block

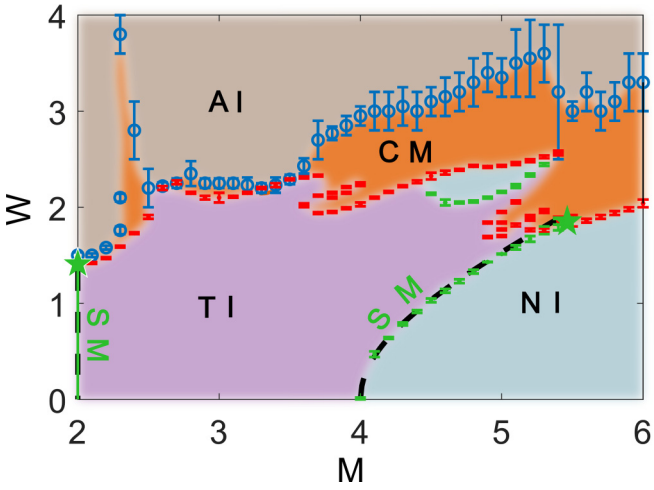

FIG. 1. Phase diagram of the Bernevig-Hughes-Zhang (BHZ) model in Eq. (1) at the band center with topological mass M and quasiperiodic potential strength W. There are five illustrated phases: topological (TI), normal (NI), and Anderson (AI) insulators, Dirac semimetal (SM), and critical metal (CM). The green and red data points use the density of states in Eq. (3) to locate the transitions between TI and NI. Among them, the green data points and the green vertical line at $M = 2$ are SMs, terminated at magic-angle transitions (see [53]) at the green stars. The black dashed lines are the perturbative prediction for the SM lines [e.g., Eq. (7)]. The blue circles use transport [Eq. (2)] to determine the CM to AI boundary.

of the BHZ model (h^*, its complex conjugate). The nonzero elements of h are $h_{\mathbf{rr}} = (M - 2t)\sigma_z$ and $h_{\mathbf{r},\mathbf{r}+\hat{\mu}} = h^\dagger_{\mathbf{r},\mathbf{r}-\hat{\mu}} = \frac{1}{2}t(-i\sigma_\mu + \sigma_z)$ for $\mu = x, y$ with Pauli matrices σ_μ. Topological mass M and the hopping $t = 1$ set the energy scale. Most analyses are done on the two-by-two matrix since time-reversal symmetry relates each block, and $V(\mathbf{r})$ does not couple blocks. To reduce finite-size effects, we average over twisted boundary conditions implemented with $t \to te^{i\tilde{\theta}_\mu/L}$ for a twist $\tilde{\theta}_\mu$ in the direction randomly sampled from $[0, 2\pi)$. The model is invariant under $M \to 4 - M$, so we focus on $M \geqslant 2$. For $2 < M < 4$, the band structure (i.e., $W = 0$) is topological with a quantized spin Hall effect $\mathcal{Q} = \sigma^+_{xy} - \sigma^-_{xy}$ where $\sigma^\pm_{xy}$ are Hall conductivities for the blocks defined by h and h^* respectively. The superscript $\pm$ will be dropped as we focus on the h block only. At $M = 2$ [$M = 4$], the model is a Dirac semimetal with Dirac points at $\mathbf{X} = (\pi, 0)$ and $\mathbf{Y} = (0, \pi)$ [$\mathbf{M} = (\pi, \pi)$] with velocity $v_0 = t$.

Quasiperiodicity is encoded in Q, which in the thermodynamic limit we define as $Q/(2\pi) = [2/(\sqrt{5}+1)]^2$. For simulations, we take rational approximates such that $Q \approx Q_L = 2\pi F_{n-2}/F_n$, where F_n is the nth Fibonacci number, and the system size is $L = F_n$. See the Supplemental Material for other values of Q [53].

Methods. We investigate the phase diagram and phase transitions with spectral observables and eigenstates. Because the model in Eq. (1) lacks translational symmetry, we treat the entire $L \times L$ system as a supercell, where the thermodynamic limit is $L \to \infty$. At finite L, we define an effective band structure that is downfolded into a mini Brillouin zone (mBZ) of size $2\pi/L \times 2\pi/L$.

We apply the kernel polynomial method (KPM) [51] to compute spectral quantities and Lanczos or exact diagonalization to compute eigenstate properties (specified in [53]). While the KPM and Lanczos work for larger L than exact diagonalization, KPM introduces broadening to the data controlled by polynomial expansion cutoff N_c [51] and Lanczos limited to a small range of the spectrum.

To distinguish trivial, topological, and Anderson insulator phases, we calculate the conductivity tensor defined through the Kubo formula [52],

$$\sigma_{\alpha\beta} = \frac{2e^2\hbar}{L^2}\int f(E)dE\,\mathrm{Im}\mathrm{Tr}\left[\!\!\left[v_\alpha \frac{dG^-}{dE} v_\beta \delta(E - H)\right]\!\!\right], \quad (2)$$

where $f(E) = [e^{\beta(E-\mu)} + 1]^{-1}$ is the Fermi function at inverse temperate β and chemical potential μ, v_α is the velocity operator, G^- is the retarded Green function, and $[[\cdots]]$ denotes an average over phases in the QP (ϕ_μ) and twists ($\tilde{\theta}_\mu$) in the boundary condition. To determine phase boundaries and transition properties, we compute the density of states (DOS) which reflects band gaps and the low energy behavior of the semimetallic phase. The DOS at energy E is

$$\rho(E) = \frac{1}{2L^2}\left[\!\!\left[\sum_i \delta(E - E_i)\right]\!\!\right], \quad (3)$$

where E_i denotes the energy eigenvalues. The gap centered at zero energy Δ is estimated with the KPM via the DOS satisfying $\rho(E) < 0.001$ and with shift-invert Lanczos about $E = 0$. Along the semimetal lines the low-energy DOS goes like $\rho(E) \sim \tilde{v}^{-2}|E|$, where $\tilde{v}$ is the renormalized velocity of the Dirac cones that we calculate through the scaling with N_c. A detailed discussion of obtaining Δ and $\tilde{v}$ is in [53].

For wave functions, we compute the inverse participation ratios (IPRs) in real and momentum space to discern localized, extended or critical states. The IPR in a basis indexed by $\boldsymbol{\alpha}$ is

$$\mathcal{I}_\alpha(E) = \sum_{\boldsymbol{\alpha}} [[|\langle \boldsymbol{\alpha}|\psi_E\rangle|^4]] \quad (4)$$

using normalized wave functions in the momentum space ($\boldsymbol{\alpha} = \mathbf{k}$) or real space ($\boldsymbol{\alpha} = \mathbf{r}$) basis. For systems localized in basis α, $\mathcal{I}_\alpha$ is L independent; for delocalized systems, it goes like $\mathcal{I}_\alpha \sim 1/L^2$. At a localization transition [54,55] $\mathcal{I}_\alpha \sim 1/L^\gamma$ where $0 < \gamma < 2$ is the fractal dimension (D_2); γ is extracted from the finite size effect when calculating $\mathcal{I}_\alpha$ at various system sizes [53].

To study band flatness and topology of the effective band structure in the mBZ, we calculate the wave unction $|\psi_{E_n}(\boldsymbol{\theta})\rangle$, where $\boldsymbol{\theta}$ is the crystal momentum of the $L \times L$ supercell (via the twist in the boundary condition as $\boldsymbol{\theta} = \tilde{\boldsymbol{\theta}}/L$) and E_n is the energy of the nth band labeled in ascending order. The bandwidth is then defined as $w_n = \max|E_n(\boldsymbol{\theta}) - E_n(\boldsymbol{\theta}')|_{\boldsymbol{\theta},\boldsymbol{\theta}'}$ and the direct band gap is $\Delta_n = E_{n+1}(\boldsymbol{\theta}) - E_n(\boldsymbol{\theta})$. The flatness ratio, which measures a band's flatness and its isolation from the neighboring bands, is defined following [14] as

$$f_n = \min\{\Delta_n, \Delta_{n-1}\}/w_n. \quad (5)$$

The Berry curvature $\Omega_n(\boldsymbol{\theta})$ and Chern number C_n can be determined via momentum-space plaquettes defined by the

four momenta $\boldsymbol{\theta} \to \boldsymbol{\theta}_1 \to \boldsymbol{\theta}_2 \to \boldsymbol{\theta}_3 \to \boldsymbol{\theta}$ [56] and they can be calculated following [57]

$$\Omega_n(\boldsymbol{\theta}) = \mathrm{Im}\ln\frac{U_n(\boldsymbol{\theta},\boldsymbol{\theta}_1)U_n(\boldsymbol{\theta}_1,\boldsymbol{\theta}_2)}{U_n(\boldsymbol{\theta},\boldsymbol{\theta}_3)U_n(\boldsymbol{\theta}_3,\boldsymbol{\theta}_2)}, \quad C_n = \frac{1}{2\pi}\sum_{\boldsymbol{\theta}}\Omega_n(\boldsymbol{\theta}), \tag{6}$$

where $U_n(\boldsymbol{\theta}_a,\boldsymbol{\theta}_b) = \langle\psi_n(\boldsymbol{\theta}_a)|\psi_n(\boldsymbol{\theta}_b)\rangle/|\langle\psi_n(\boldsymbol{\theta}_a)|\psi_n(\boldsymbol{\theta}_b)\rangle|$ and the sum to obtain C_n is over the mBZ $[0, 2\pi/L)^2$. Last, we use machine learning of the wave functions to provide an efficient survey of a large parameter space (in W, M, and E) as an additional validation of the phase diagram in Fig. 1. This also reveals intriguing features of the Anderson insulating phase, as elaborated in [53].

Phase diagram. Using diagrammatic perturbation theory and numerical calculations with the KPM and Lanczos we obtain the phase diagrams shown in Fig. 1. There are five phases pictured: topological insulator (TI), normal insulator (NI), critical metal (CM), Anderson insulator (AI), and lines of Dirac semimetals (SMs) between TI and NI phases. Both band-insulating and SM phases are stable to weak quasiperiodicity. Finite band gaps and quantized (zero) spin Hall conductivity describe the TI (NI) phase, calculated using the KPM method with Eq. (2). Low-energy scaling of the DOS $\rho(E) \sim \tilde{v}^{-2}|E|$ captures the SM phases (marked with green data points). Other boundaries between gapped and finite DOS at $E = 0$ are marked with red data points. These DOS results trace the phase boundaries between TI and NI (green) and between TI and CM (red). The AI phase has a finite DOS but zero conductivity and localized wave functions (i.e., real space IPR that is L independent), with the phase boundary marked by blue circles with error bars. The structure revealed is Q dependent [53] and reminiscent of other studies of insulating phases perturbed by quasiperiodicity [58].

Upon increasing W, for $M \lesssim 4$ and $M \gtrsim 5$ we traverse the phases TI/NI $\to$ CM $\to$ AI. However, more complicated cuts are possible between $M = 4.5$ and $M = 5.3$, where quasiperiodicity drives trivial phases topological (for $4 < M \lesssim 5.0$) and into and out of metallic and topological phases at zero energy. An example is shown in the Supplemental Material [53], where increasing W leads to the phases NI $\to$ SM $\to$ TI $\to$ CM $\to$ TI $\to$ SM $\to$ NI $\to$ CM $\to$ AI.

The physics on the SM lines emanating from $M = 2$ or $M = 4$ at $W = 0$ agrees with the universal features found in Ref. [31] and reveals magic-angle transitions marked by green stars in Fig. 1(a). Concentrating on $M = 2$, the semimetal is stable with a velocity (calculated from the DOS, see [53]) that vanishes like $\tilde{v} \sim [W_c(M = 2) - W]^{\beta/2}$ where $W_c(M = 2) = 1.42 \pm 0.02$ and $\beta = 2 \pm 0.3$, which is close to the universal value $\beta \approx 2$ obtained in other models and symmetry classes [31,32]. A CM phase is found as well as a localization transition at $W_A(M = 2) = 1.50 \pm 0.03$.

For smaller values of W, we use perturbation theory to map out the phase diagram and estimate the location of the NI-to-TI and SM-to-CM transitions (see [53]). These phase transitions can be assessed in this regime (i.e., near $M = 4$) by computing the renormalized mass $\tilde{M}$ and velocity $\tilde{v}$. We obtain up to second order in W,

$$\tilde{M} - 4 = \frac{\left[(M-4) + W^2\frac{(4-M)+(\cos Q-1)}{(4-M)^2+2(3-M)(\cos Q-1)}\right]}{1 + W^2/[(4-M)^2 + 2(3-M)(\cos Q - 1)]}. \tag{7}$$

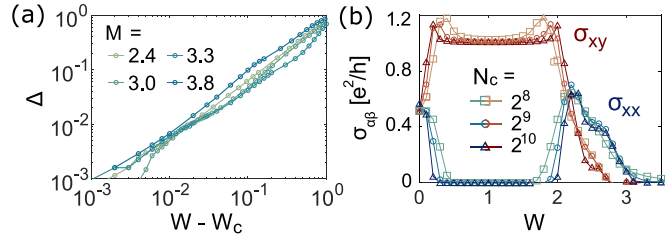

FIG. 2. Demonstration of the TI-to-CM transition. (a) Tracking the density of states computed with the KPM in Eq. (3), we see the (hard) band gap closes as a power law $\Delta = [W_c(M) - W]^{\nu z}$ and find $\nu z \approx 1$ at the TI-to-CM transition across each value of M. Panel (b) shows the conductivity computed with the KPM in Eq. (2) as a function of quasiperiodic strength W for $M = 4.0$. The Hall conductivity σ_{xy} saturates to a finite value in the TI phase, but for $W_c(M = 4) \approx 2 \lesssim W \lesssim 3$ the longitudinal conductivity becomes finite and the Hall part is suppressed. The system is localized when $W \gtrsim 3$. Note that the feature near $W = 0$ is due to $M = 4$ being a SM. We stress that this metallic phase and therefore this transition does not exist in the presence of randomness.

By solving for $\tilde{M} = 4$, we obtain the phase boundary between insulating phases, illustrated by the black dotted line in Fig. 1(a) (at fourth order in W), which is in excellent agreement with the numerics. The curvature to this line demonstrates that quasiperiodicity can drive a topological phase transition NI to TI, which is the deterministic analog of the disordered topological Anderson insulator [59,60]. For $M = 2$, there is no renormalization of $\tilde{M}$. Using numerics to access higher M and W, when $M \gtrsim 5.4$, the NI transitions into the CM. The magic-angle transition (i.e., SM to CM) is obtained by solving $\tilde{v} \to 0$ on the line $\tilde{M} = 4$.

TI-to-CM transition. To analyze topological transitions that are forbidden in disorder systems we use numerics to capture the full, nonperturbative transition to the CM phase located at $W_c(M)$. Near the transition, the correlation length diverges as $\xi \sim |W - W_c|^{-\nu}$ while scale invariance implies that the gap $\Delta \sim \xi^{-z}$; therefore the gap vanishes like $\Delta \sim |W - W_c|^{\nu z}$. Through the KPM calculation of DOS and Lanczos calculation of lowest energy states, we find $\nu z \approx 1$ for each M value we have considered; see Fig. 2(a).

These exponents indicate a unique universality class driven by quasiperiodicity distinct from random systems. Since our system breaks up into two blocks, each in the same symmetry class as the quantum Hall effect (i.e., class A), random disorder does not allow for a metallic phase [41,55,61]. Therefore, topological phase transitions driven by quasiperiodicity host unique universality classes beyond the ten Altland-Zirnbauer random matrix classes [40].

When the gap closes at $W_c(M)$, the conductivity at $E = 0$ becomes finite, and the Hall conductivity is no longer quantized, indicating the onset of the CM phase. As seen in Fig. 2(b), the Hall conductivity drops, and σ_{xx} peaks at the transition, remaining finite for the duration of the CM. The transition does not involve any symmetry breaking; it occurs when the topological gap closes and σ_{xy} is no longer quantized. For larger values of W, we find a transition into an Anderson insulating phase [55,62] with exponentially localized wave functions in real space and a vanishing σ_{xx}.

Criticality and flat topological bands. At small W, the insulating band gap [computed via the DOS in Eq. (3)] increases for some values of M but decreases for larger W, which is beyond the perturbative theory in Eq. (7). This nonmonotonicity is demonstrated in [53] and coincides with the onset of criticality in the finite energy states (i.e., a mobility edge) near the edge of the gap centered about $E = 0$ (e.g., in Fig. 3 this corresponds to the states near $E \approx -0.5$ for $W \approx 1$). Due to the interplay of topology, criticality, and quasiperiodicity several physically interesting effects occur near the gap maximum. This is demonstrated in Fig. 3 for $M = 4.0$ as a representative cut of the phase diagram in Fig. 1 that we now explore in more detail.

It can be seen from Fig. 3(a) that the states [63] near $E \approx -0.5$ narrow around $W \approx 1$ and are well isolated from other states by hard gaps. Additionally, by calculating σ_{xy}, Fig. 3(b) (leftmost panel) shows that this collection of bands has a total Chern number equal to 1, independent of L. Meanwhile, these states become critical, as measured by the IPR in momentum and position space ($1/\mathcal{I}_\alpha \approx L^{\gamma_\alpha}$) with $0 < \gamma_\alpha < 2$, showing that they are delocalized in both bases ($\alpha = x, k$) [Fig. 3(a) where color shows γ_k]. Interestingly, we observe a self-similarity in these critical bands; the sequence of decreasing energy windows shown in Fig. 3(b) have the same Chern number as we increase the supercell size. When $M = 4$ and $W = 1.015\,41$ the relevant energy window $E \in [-0.49, -0.47]$ has $(F_{n-5})^2$ states for a system size $L = F_n$. When we can identify the lowest band [depicted by the green line in Fig. 3(b)] in this energy window the value of its Chern number follows the self-similar sequence of $C = -2$ for $L = F_{2n}$ and $C = 1$ for $L = F_{2n-1}$ (in each case examined).

The flatness of the lowest (green) band is apparent in the dispersion in the mBZ in Fig. 3(b) as well as by its large effective mass [53]. By computing the flatness ratio (of the green band) f_g and Berry curvature Ω_g [in Eqs. (5) and (6), respectively] our data also demonstrate that larger L leads to flatter, isolated topological bands in the mBZ at some optimal W. As shown in Figs. 3(b) and 3(c), left, for increasing L the peak in f_g sharpens concomitantly with the development of critical eigenstates [Fig. 3(a)] as the Chern bands in the mBZ occur at an increasingly fine energy scale. At the W with maximal f_g, we also see a reduction in the fluctuation in Berry curvature Ω_g (of the green band), probed via its standard deviation divided by the mean across the mBZ [53], Fig. 3(c), right. The reduction of fluctuations of Ω_g for increasing L suggests that the model could host a fractional Chern insulating state in the presence of interactions [64,65]; however, it is possible that an incommensurate charge density wave state could be stabilized instead (see [53] for Berry curvature profiles in the mBZ).

Conclusion. This simple two-dimensional model of a TI shows how quasiperiodicity can induce flat bands, eigenstate criticality, and phases outside the AZ disordered classification. This not only has implications for correlated physics but to twisted heterostructures, ultracold atoms, and metamaterials—all of which have realized 2D TIs [33–39]. In fact, these metallic phases should show up in experiments of density and time-of-flight measurements (to see delocalization in real and momentum space, respectively) and the phase diagram can be obtained from transport experiments [66]

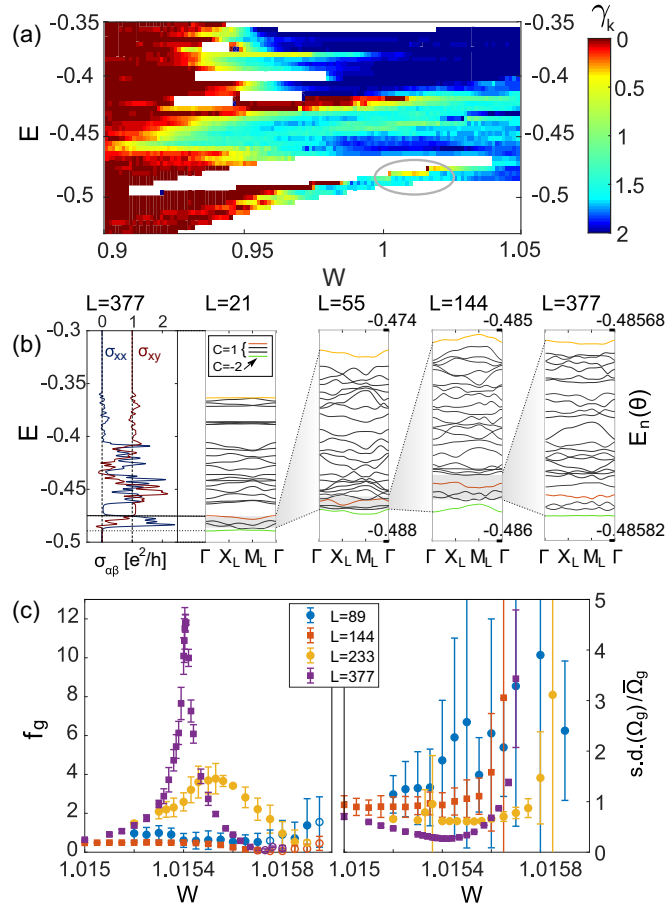

FIG. 3. Flat Chern bands and eigenstate criticality. (a) Plot of the Momentum-space IPR system-size scaling [as defined in Eq. (4)]. Notice that around $W \sim 0.95$ low energies become delocalized in momentum space while at higher energies $\mathcal{I}_k \sim L^{-\gamma_k}$ for $0 < \gamma_k < 2$ indicating critical eigenstates along the mobility edge; the value of γ_k is given by the color. The lowest energy states (and narrowest set of states) has a Chern number of 1. The white regions are hard gaps. (b) Left: Conductivity calculated from Eq. (2) with $L = 377$ and cutoff $N_c = 2^{14}$. Right: Dispersion relation $E_n(\boldsymbol{\theta})$ along a representative cut in the mBZ for a sequence of $L = F_n$ with even n, for $W = 1.0154$. For each L, the green band carries Chern number -2, the first four bands (from green to cyan) sum to Chern number 1, and the 25 bands pictured in each plot sum to Chern number 1 (for $L = 55$, the pattern appears to hold but the lowest bands do not have a well-defined gap). (c) Flatness ratio f_g [left, as defined in Eq. (5)] and the normalized standard deviation of Berry curvature Ω_g [as defined in Eq. (6)] across the folded Brillouin zone (right) of the first band above $E = -0.5$, for various L values. For $L = 233$ and $L = 377$, the peak of the flatness ratio appears near where the Berry curvature has less fluctuations. The filled markers (•) indicate topological bands while empty markers (○) indicate trivial bands (excluded in the right). The squares (■) and circles (•) correspond to $L = F_n$ such that n is odd and even, respectively.

and spectral function measurements [67] in cold atomic systems, and absorption in metamaterials of microwave resonator arrays.

Acknowledgments. We thank Y. Barlas, E. König, and J. Wang for useful discussions. This work was partially supported by Grant No. 2018058 from the United States-Israel

Binational Science Foundation (BSF), NSF CAREER Grant No. DMR-1941569, and by the Air Force Office of Scientific Research under Grant No. FA9550-20-1-0136. Numerical calculations were done using JULIA [68]. The authors acknowledge the following research computing resources that have contributed to the results reported here: the Open Science Grid [69,70], supported by National Science Foundation Award No. 1148698, and the U.S. Department of Energy Office of Science, the Beowulf cluster at the Department of Physics and Astronomy of Rutgers University; and the Office of Advanced Research Computing (OARC) at Rutgers, The State University of New Jersey [71], is acknowledged for providing access to the Amarel cluster. The Flatiron Institute is a division of the Simons Foundation.

[1] H. L. Stormer, D. C. Tsui, and A. C. Gossard, Rev. Mod. Phys. **71**, S298 (1999).
[2] J. Maciejko and G. A. Fiete, Nat. Phys. **11**, 385 (2015).
[3] N. Regnault and B. A. Bernevig, Phys. Rev. X **1**, 021014 (2011).
[4] Z. Liu, E. J. Bergholtz, H. Fan, and A. M. Läuchli, Phys. Rev. Lett. **109**, 186805 (2012).
[5] F. Harper, S. H. Simon, and R. Roy, Phys. Rev. B **90**, 075104 (2014).
[6] M. A. Bandres, M. C. Rechtsman, and M. Segev, Phys. Rev. X **6**, 011016 (2016).
[7] J. Maciejko, X.-L. Qi, A. Karch, and S.-C. Zhang, Phys. Rev. Lett. **105**, 246809 (2010).
[8] B. Swingle, M. Barkeshli, J. McGreevy, and T. Senthil, Phys. Rev. B **83**, 195139 (2011).
[9] E. J. Bergholtz and Z. Liu, Int. J. Mod. Phys. B **27**, 1330017 (2013).
[10] S. A. Parameswaran, R. Roy, and S. L. Sondhi, C. R. Phys. **14**, 816 (2013).
[11] Y.-F. Wang, H. Yao, C.-D. Gong, and D. N. Sheng, Phys. Rev. B **86**, 201101(R) (2012).
[12] S. Yang, Z.-C. Gu, K. Sun, and S. Das Sarma, Phys. Rev. B **86**, 241112(R) (2012).
[13] T. T. Heikkilä, N. B. Kopnin, and G. E. Volovik, JETP Lett. **94**, 233 (2011).
[14] C. H. Lee, D. P. Arovas, and R. Thomale, Phys. Rev. B **93**, 155155 (2016).
[15] C. H. Lee, M. Claassen, and R. Thomale, Phys. Rev. B **96**, 165150 (2017).
[16] Y. Cao, V. Fatemi, A. Demir, S. Fang, S. L. Tomarken, J. Y. Luo, J. D. Sanchez-Yamagishi, K. Watanabe, T. Taniguchi, E. Kaxiras *et al.*, Nature (London) **556**, 80 (2018).
[17] Y. Cao, V. Fatemi, S. Fang, K. Watanabe, T. Taniguchi, E. Kaxiras, and P. Jarillo-Herrero, Nature (London) **556**, 43 (2018).
[18] M. Yankowitz, S. Chen, H. Polshyn, Y. Zhang, K. Watanabe, T. Taniguchi, D. Graf, A. F. Young, and C. R. Dean, Science **363**, 1059 (2019).
[19] A. L. Sharpe, E. J. Fox, A. W. Barnard, J. Finney, K. Watanabe, T. Taniguchi, M. Kastner, and D. Goldhaber-Gordon, Science **365**, 605 (2019).
[20] J. H. Pixley and E. Y. Andrei, Science **365**, 543 (2019).
[21] H. Polshyn, J. Zhu, M. Kumar, Y. Zhang, F. Yang, C. Tschirhart, M. Serlin, K. Watanabe, T. Taniguchi, A. MacDonald *et al.*, Nature (London) **588**, 66 (2020).
[22] Y.-H. Zhang, D. Mao, Y. Cao, P. Jarillo-Herrero, and T. Senthil, Phys. Rev. B **99**, 075127 (2019).
[23] B. L. Chittari, G. Chen, Y. Zhang, F. Wang, and J. Jung, Phys. Rev. Lett. **122**, 016401 (2019).
[24] F. Wu, Phys. Rev. B **99**, 195114 (2019).
[25] T. M. R. Wolf, O. Zilberberg, I. Levkivskyi, and G. Blatter, Phys. Rev. B **98**, 125408 (2018).
[26] Q. Tong, H. Yu, Q. Zhu, Y. Wang, X. Xu, and W. Yao, Nat. Phys. **13**, 356 (2017).
[27] P. San-Jose, A. Gutiérrez-Rubio, M. Sturla, and F. Guinea, Phys. Rev. B **90**, 115152 (2014).
[28] B. Lian, Z. Liu, Y. Zhang, and J. Wang, Phys. Rev. Lett. **124**, 126402 (2020).
[29] P. J. Ledwith, G. Tarnopolsky, E. Khalaf, and A. Vishwanath, Phys. Rev. Res. **2**, 023237 (2020).
[30] Z. Song, Z. Wang, W. Shi, G. Li, C. Fang, and B. A. Bernevig, Phys. Rev. Lett. **123**, 036401 (2019).
[31] Y. Fu, E. J. König, J. H. Wilson, Y.-Z. Chou, and J. H. Pixley, npj Quantum Mater. **5**, 71 (2020).
[32] Y.-Z. Chou, Y. Fu, J. H. Wilson, E. König, and J. Pixley, Phys. Rev. B **101**, 235121 (2020).
[33] C. J. Kennedy, G. A. Siviloglou, H. Miyake, W. C. Burton, and W. Ketterle, Phys. Rev. Lett. **111**, 225301 (2013).
[34] L. Huang, Z. Meng, P. Wang, P. Peng, S.-L. Zhang, L. Chen, D. Li, Q. Zhou, and J. Zhang, Nat. Phys. **12**, 540 (2016).
[35] Z. Wu, L. Zhang, W. Sun, X.-T. Xu, B.-Z. Wang, S.-C. Ji, Y. Deng, S. Chen, X.-J. Liu, and J.-W. Pan, Science **354**, 83 (2016).
[36] R. Süsstrunk and S. D. Huber, Science **349**, 47 (2015).
[37] E. Lustig, S. Weimann, Y. Plotnik, Y. Lumer, M. A. Bandres, A. Szameit, and M. Segev, Nature (London) **567**, 356 (2019).
[38] C. W. Peterson, W. A. Benalcazar, T. L. Hughes, and G. Bahl, Nature (London) **555**, 346 (2018).
[39] S. Imhof, C. Berger, F. Bayer, J. Brehm, L. W. Molenkamp, T. Kiessling, F. Schindler, C. H. Lee, M. Greiter, T. Neupert, and R. Thomale, Nat. Phys. **14**, 925 (2018).
[40] A. Altland and M. R. Zirnbauer, Phys. Rev. B **55**, 1142 (1997).
[41] A. Yamakage, K. Nomura, K.-I. Imura, and Y. Kuramoto, Phys. Rev. B **87**, 205141 (2013).
[42] T. Devakul and D. A. Huse, Phys. Rev. B **96**, 214201 (2017).
[43] J. H. Pixley, J. H. Wilson, D. A. Huse, and S. Gopalakrishnan, Phys. Rev. Lett. **120**, 207604 (2018).
[44] H. Huang and F. Liu, Phys. Rev. B **98**, 125130 (2018).
[45] H. Huang and F. Liu, Phys. Rev. Lett. **121**, 126401 (2018).
[46] D.-T. Tran, A. Dauphin, N. Goldman, and P. Gaspard, Phys. Rev. B **91**, 085125 (2015).
[47] D. Mao and S. Todadri, Phys. Rev. B **103**, 115110 (2021).
[48] T. Cea, P. A. Pantaleón, and F. Guinea, Phys. Rev. B **102**, 155136 (2020).
[49] J. Shi, J. Zhu, and A. H. MacDonald, Phys. Rev. B **103**, 075122 (2021).
[50] B. A. Bernevig, T. L. Hughes, and S.-C. Zhang, Science **314**, 1757 (2006).

[51] A. Weiße, G. Wellein, A. Alvermann, and H. Fehske, Rev. Mod. Phys. **78**, 275 (2006).
[52] J. H. García, L. Covaci, and T. G. Rappoport, Phys. Rev. Lett. **114**, 116602 (2015).
[53] See Supplemental Material at http://link.aps.org/supplemental/10.1103/PhysRevB.104.L041106 for additional details on the phase diagram as well as the analytical and numerical methods used (which includes Refs. [72–77] on machine learning).
[54] A. D. Mirlin, Phys. Rep. **326**, 259 (2000).
[55] F. Evers and A. D. Mirlin, Rev. Mod. Phys. **80**, 1355 (2008).
[56] All plaquettes must be chosen with the same orientation.
[57] T. Fukui, Y. Hatsugai, and H. Suzuki, J. Phys. Soc. Jpn. **74**, 1674 (2005).
[58] G. Roux, T. Barthel, I. P. McCulloch, C. Kollath, U. Schollwöck, and T. Giamarchi, Phys. Rev. A **78**, 023628 (2008).
[59] C. W. Groth, M. Wimmer, A. R. Akhmerov, J. Tworzydło, and C. W. J. Beenakker, Phys. Rev. Lett. **103**, 196805 (2009).
[60] E. J. Meier, F. A. An, A. Dauphin, M. Maffei, P. Massignan, T. L. Hughes, and B. Gadway, Science **362**, 929 (2018).
[61] C.-Z. Chen, H. Liu, H. Jiang, Q.-F. Sun, Z. Wang, and X. C. Xie, Phys. Rev. B **91**, 214202 (2015).
[62] E. Abrahams, P. W. Anderson, D. C. Licciardello, and T. V. Ramakrishnan, Phys. Rev. Lett. **42**, 673 (1979).
[63] By downfolding this collection of states originated from a band at a given L.
[64] S. A. Parameswaran, R. Roy, and S. L. Sondhi, Phys. Rev. B **85**, 241308(R) (2012).
[65] M. Claassen, C. H. Lee, R. Thomale, X.-L. Qi, and T. P. Devereaux, Phys. Rev. Lett. **114**, 236802 (2015).
[66] S. Krinner, T. Esslinger, and J.-P. Brantut, J. Phys.: Condens. Matter **29**, 343003 (2017).
[67] J. P. Gaebler, J. T. Stewart, T. E. Drake, D. S. Jin, A. Perali, P. Pieri, and G. C. Strinati, Nat. Phys. **6**, 569 (2010).
[68] J. Bezanson, A. Edelman, S. Karpinski, and V. B. Shah, SIAM Rev. **59**, 65 (2017).
[69] R. Pordes, D. Petravick, B. Kramer, D. Olson, M. Livny, A. Roy, P. Avery, K. Blackburn, T. Wenaus, F. Würthwein, I. Foster, R. Gardner, M. Wilde, A. Blatecky, J. McGee, and R. Quick, J. Phys.: Conf. Ser. **78**, 012057 (2007).
[70] I. Sfiligoi, D. C. Bradley, B. Holzman, P. Mhashilkar, S. Padhi, and F. Wurthwein, in *2009 WRI World Congress on Computer Science and Information Engineering* (IEEE, Los Angeles, 2009), Vol. 2, pp. 428–432.
[71] http://oarc.rutgers.edu
[72] A. Krizhevsky, I. Sutskever, and G. E. Hinton, in *Advances in Neural Information Processing Systems* (2012), pp. 1097–1105.
[73] C. M. Bishop, *Pattern Recognition and Machine Learning* (Springer, New York, 2006).
[74] G. E. Hinton, N. Srivastava, A. Krizhevsky, I. Sutskever, and R. R. Salakhutdinov, arXiv:1207.0580.
[75] T. Ohtsuki and T. Ohtsuki, J. Phys. Soc. Jpn. **85**, 123706 (2016).
[76] J. Carrasquilla and R. G. Melko, Nat. Phys. **13**, 431 (2017).
[77] P. Baldi, P. Sadowski, and D. Whiteson, Nat. Commun. **5**, 4308 (2014).